ACES Asian Chemical Editorial Society

doi.org/10.1002/asia.202401735

CHEMISTRY AN ASIAN JOURNAL Research Article

www.chemasianj.org

Photophysical and Chiroptical Properties of Pyrazino-Phenanthroline-Helicene Derivative and its Rhenium(I) Complex

Debsouri Kundu[+],[a] Dominika Jelonek[+],[b, c] Natalia Del Rio,[a] Nicolas Vanthuyne,[d] Monika Srebro-Hooper,*[b] and Jeanne Crassous*[a]

A novel coordination motif comprising [4]helicene fused with pyrazino-phenanthroline (**H4PP**) has been synthesized and reacted with $ReCl(CO)_5$ to yield its rhenium(I) complex (**Re-H4PP**). Absorption and emission spectroscopic analysis conducted in dichloromethane and 2-methyltetrahydrofuran reveals that combining pyrazino-phenanthroline with helicene visibly affects the photophysical attributes of both the resulting ligand and its Re(I) complex as compared to their non-helicene analogues, and even more importantly leads to relatively high photoluminescence quantum yield values, especially in the case of **H4PP** (29%). Chiroptical studies through electronic circular dichroism and circularly polarized luminescence performed on enantiomerically enriched samples of **Re-H4PP** show the chiral nature of low-energy excited states affording notable g_{lum} values that amplify at cryogenic temperatures. Insights into experimental results are provided *via* first-principles quantum-chemical calculations showing important role of intra-ligand charge-transfer (ILCT) and metal-to-ligand CT (MLCT) states in determining photophysical features of these systems.

Introduction

Polypyridyl metal complexes incorporating pyrazino-phenanthroline (PP) derivatives present a wide array of properties including photophysical and biological activities. Typical examples are (b)dppz-based complexes ((b)dppz = (benzo[h])dipyrido[3,2-a:2′,3′-c]phenazine) that can intercalate to DNA, a property which can be followed by time-resolved spectroscopies through long-lived triplet excited states. For instance, Ru-(b)dppz[1] and Re-dppz[2] complexes were shown to be efficient intercalators, undergoing light switching and electron transfer phenomena. Interestingly, intra-ligand, ^{3}IL($\pi\pi^*$), and metal-to-ligand charge-transfer, ^{3}MLCT, triplet states were suggested to explain the photophysics of these Ru(II) and Re(I) (b)dppz-based complexes. Furthermore, PP derivatives have been used to develop efficient UV-Vis-NIR luminescent organic molecules and coordination complexes with a variety of lanthanides and transition metals[3] for applications in organic light-emitting diodes (OLEDs).[4,5]

In the present work, we report on the first helical pyrazino-phenanthroline ligand, namely [4]helicene-pyrazino[2,3-*f*][1,10]phenanthroline (**H4PP**) obtained from simple condensation of a 1,2-[4]helicene-diamine with 1,10-phenanthroline-5,6-dione (Scheme 1). The corresponding $Re(CO)_3Cl$ complex (**Re-H4PP**) was then prepared and its stereochemical features associated with the helical PP ligand and chiral rhenium center were analyzed. Through absorption and emission spectroscopies at room and low temperatures, along with lifetime measurements, we probed low-lying excited states in both the ligand and its Re(I) complex. Furthermore, chirality associated with these states was investigated by employing electronic circular dichroism (ECD) and circularly polarized luminescence (CPL) spectroscopies on enantiomerically enriched samples of **Re-H4PP**. Theoretical computations employing (time-dependent) density functional theory ((TD)DFT)[6] with spin-orbit coupling (SOC) offered insights into electronic structure and nature of the electronic transitions underlying observed spectroscopic characteristics, including mechanism of populating of triplet states manifold *via* intersystem crossing (ISC) path. By combining the unique architecture and chirality of helicene with the electronic features of pyrazino-phenanthroline moiety we accordingly unveil a new type of helicene rhenium(I) complex and study the fundamental chemistry governing its properties by a blend of experimental and computational analyses.

[a] *D. Kundu,[+] N. Del Rio, J. Crassous*
Institut des Sciences Chimiques de Rennes, University of Rennes, CNRS, ISCR, UMR 6226, F-35000 Rennes, France
E-mail: jeanne.crassous@univ-rennes.fr

[b] *D. Jelonek,[+] M. Srebro-Hooper*
Faculty of Chemistry, Jagiellonian University, Gronostajowa 2, 30-387 Krakow, Poland
E-mail: monika.srebro@uj.edu.pl

[c] *D. Jelonek[+]*
Doctoral School of Exact and Natural Sciences, Jagiellonian University, Prof. St. Łojasiewicza St 11, 30-348 Cracow, Poland

[d] *N. Vanthuyne*
Aix Marseille Univ, CNRS, Centrale Med, FSCM, Marseille, France

[+] *These authors contributed equally to the work.*

Supporting information for this article is available on the WWW under https://doi.org/10.1002/asia.202401735

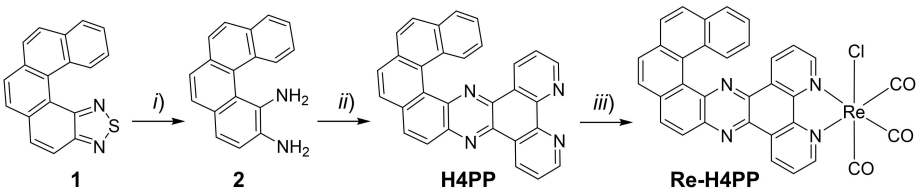

Scheme 1. Synthesis of **H4PP** and its Re(I) complex **Re-H4PP**: *i*) $LiAlH_4$, THF, 0 °C – rt, Ar, 5 hrs; *ii*) toluene, 1,10-phenanthroline-5,6-dione (1.5 eq.), *p*-toluenesulfonic acid (cat.), reflux, 18 hrs, 60%; *iii*) $Re(CO)_5Cl$ (1.0 eq.), toluene, reflux, 18 hrs, 67%.

Results and Discussion

Synthesis

Thiadiazole derivatives are heterocyclic compounds belonging to the azole class, possessing two carbon atoms, two nitrogen atoms, and one sulfur atom within the same ring. They exhibit remarkable chemical versatility and photophysical properties.[7] 1,2,5-Thiadiazoles can be easily reduced to produce 1,2-bis-amines, which work as precursors for a number of important organic units through simple condensation reactions.[8]

Utilizing [5]helicene-thiadiazole **1** as a precursor,[9] 1,2-[4]helicene-diamine was prepared *in situ* as previously reported by our group (Scheme 1).[10] A condensation reaction in refluxing toluene between **2** and 1,10-phenanthroline-5,6-dione catalyzed by *p*-toluenesulfonic acid yielded **H4PP** integrating the phenanthroline motif within the helicenic backbone. Coordination of Re(I) to **H4PP** was then achieved by the reaction with $ReCO_5Cl$ in refluxing toluene, resulting in a complex with significantly reduced solubility at room temperature that facilitated precipitation-based isolation. Detailed ^1H and ^{13}C NMR spectra and mass spectrometry are provided in the Supplementary Information (SI).

A comparison of ^1H NMR spectra between the ligand **H4PP** and its rhenium(I) complex **Re-H4PP** reveals reduction in the electron density upon metal coordination. The incorporation of the Re(I) center into **H4PP** induces a notable downfield shift in the entire spectrum, with an observed maximum displacement of up to 0.2 ppm (see SI). The most pronounced deshielding effect is exhibited by protons adjacent to the nitrogen atoms within the phenanthroline framework. In contrast, protons located on the peripheral ring of the helicene structure exhibit a more modest shift, ranging between 0.03 ppm and 0.1 ppm. This differential response underscores that proximity to the metal center plays a pivotal role in influencing the reorganization of electronic distribution over the ligand scaffold due to donation/back-donation bonding processes. Such observations are well-documented in coordination chemistry and are consistent with previous reports on helicene-bipyridine systems.[11]

Despite our best efforts, attempts to separate the (*P*) and (*M*) enantiomers of **H4PP** were found to be unsuccessful. However, despite its poor solubility, we managed to obtain enantiomerically enriched samples of **Re-H4PP** complex on an analytical scale, utilizing chiral HPLC. Namely, employing a Chiralpak IH column (hexane, ethanol, and dichloromethane in a 6:2:2 ratio as mobile phase, see the SI) effective separation of **Re-H4PP** into two distinct enantiomeric fractions was achieved, for which a decisive assignment of (*P*) and (*M*) helical configuration was supported by the performed (TD)DFT calculations (*vide infra*). It should be however noted that these (*P*) and (*M*) enantiomers can exist in two octahedral diastereomeric forms, which differ in the configuration at the Re(I) metal center (C_{Re} and A_{Re}). Nonetheless, both size-exclusion chromatography and chiral HPLC, a technique historically successful in diastereomeric separation of chiral molecular systems including the previously reported rhenium(I)-helicene complexes,[11,12] failed to distinguish between these configurations. This outcome suggests an insufficient size difference between the diastereomers, their potential dynamic equilibrium in solution, or a preferential formation of one stereoisomer under the synthetic conditions employed. Selective formation has not been previously observed for monometallic systems but seen, for example, in dirhenium-helicene-bipyridine complexes.[11b]

Optimized Geometries and Electronic Structure

The optimized ground-state geometries of the helicene-pyrazino-phenanthroline ligand (*P*)-**H4PP** along with its corresponding Re(I) complex – considered in two possible diastereomeric forms – (P,C_{Re})-**Re-H4PP^I** and (P,A_{Re})-**Re-H4PP^{II}** are presented in Figure 1. See the SI for a description of computational details employed in the studies reported herein and a full set of calculated data including those obtained also for the model (non-helicenic) reference systems. The angle between the

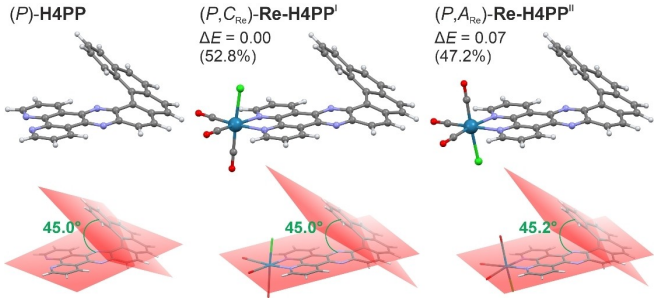

Figure 1. Top: DFT-optimized (B3LYP/def2-TZVP with a continuum solvent (dichloromethane) model) structures of (*P*)-**H4PP**, (P,C_{Re})-**Re-H4PP^I**, and (P,A_{Re})-**Re-H4PP^{II}**. Numbers listed are the corresponding relative electronic energy ΔE values (in kcal/mol) along with the respective Boltzmann populations at 298 K (in parentheses). Bottom: Measured angles between pyrazine ring and helicene terminal ring.

terminal rings of pentahelicene fragment is *ca.* 45° for both **H4PP** and **Re-H4PP** structures, which corresponds to the classical pentahelicene value.[13] In rhenium complex, the phenanthroline segment retains a planar conformation, seamlessly extending into the rhenium's basal plane, which includes two carbonyl groups. The Re(I) metal center assumes an octahedral geometry, in which the chlorine atom takes an apical position with its two possible arrangements relative to the helicene backbone. Namely, in (P,C_{Re})-**Re-H4PP^{I}** diastereomer, Cl is oriented towards the helicene, while in (P,A_{Re})-**Re-H4PP^{II}**, it is positioned away from helicene (Figure 1). Within the numerical accuracy of the DFT energy and free-energy calculations, these two diastereomers appear to be isoenergetic, showing nearly equal (*ca.* 50%) Boltzmann populations at 298 K, which reflects large spatial separation between Cl/CO and helicenic moiety in (P,C_{Re})-**Re-H4PP^{I}**/(P,A_{Re})-**Re-H4PP^{II}**. The similar molecular size of both these diastereomers along with their comparable thermodynamical stability, demonstrated by the calculations, may explain their unsuccessful separation *via* size-exclusion chromatography or chiral HPLC, contrary to the previously reported Re(I)-helicene complexes.[11,12]

An analysis of molecular orbitals (MOs) was performed to comment on the extent of π-electron conjugation in both the pristine ligand and upon its binding to Re(I) ion. Isosurfaces of the frontier MOs (FMOs) for (P)-**H4PP** and (P,C_{Re})-**Re-H4PP^{I}** are depicted in Figure 2 top; note that the corresponding molecular orbitals of the two diastereomers of **Re-H4PP** are essentially visually identical. For a full set of computed data, see the SI (Figures S2.9–11). As can be seen in Figure 2, the **H4PP** ligand is characterized by π-conjugated electron system delocalized over

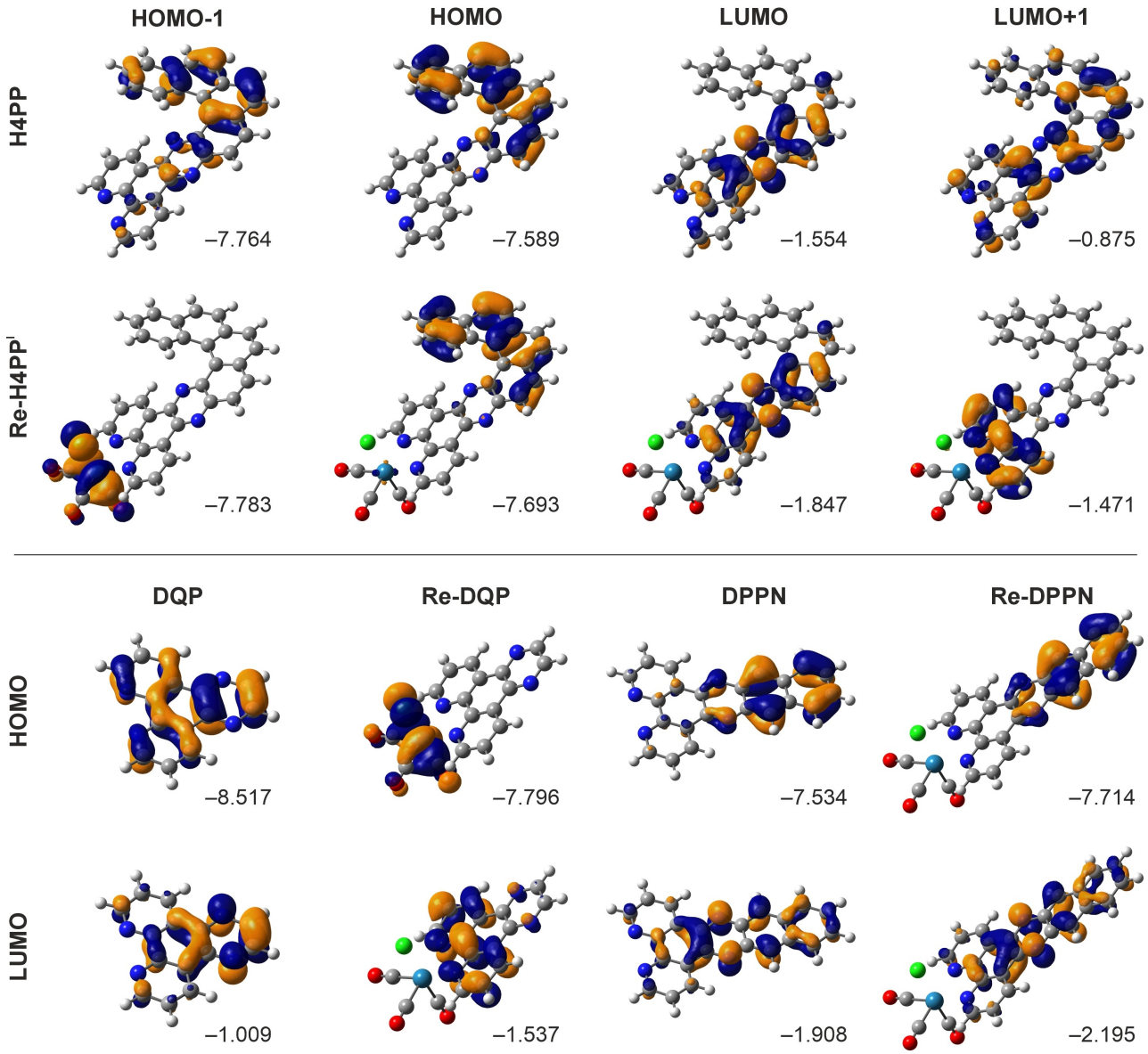

Figure 2. Isosurfaces (±0.04 au) of FMOs of (P)-**H4PP** and (P,C_{Re})-**Re-H4PP^{I}** (top) and of **DQP** (dipyrido[3,2-f:2′,3′-h]quinoxaline), **DPPN** (benzo[i]dipyrido[3,2-a:2′,3′-c]phenazine), **Re-DQP** and **Re-DPPN** (bottom) obtained based on LC-PBE0*/def2-TZVP/PCM(CH_2Cl_2) calculations. Values listed are the corresponding orbital energies (in eV). See the SI for a full set of computed data.

both pyrazino-phenanthroline and helicene moieties, although π-density in HOMO and LUMO shows a clear spatial separation as it is localized mainly at H4 and at PP with adjacent helicenic benzene ring, respectively. This may pave the way for low-energy intra-ligand charge-transfer (ILCT) excited states. The effect of the enlargement of the π-electron system with the corresponding polarization of its density is clearly visible comparing the **H4PP** MOs with those for the model (non-helicenic) systems (for structures visualization, see Table 1 and Figure S2.1; for MOs visualization, see Figure 2 bottom and Figures S2.12–13). In particular, it can be noted that for the HOMO orbital, an increase in the number of the benzene rings fused with pyrazine leads to a depletion of the π-electron density from the phenanthroline fragment. Namely, in **DQP** (dipyrido[3,2-f:2′,3′-h]quinoxaline), HOMO is delocalized over the whole molecule, in **DPPN** (benzo[i]dipyrido[3,2-a:2′,3′-c]phenazine) – localized mostly at pyrazine-naphthalene rings, while in **H4PP**, as aforementioned, it spreads almost exclusively over helicene. Regarding the LUMO orbitals, for **DPPN**, as expected, it reflects extended π-conjugation across the molecule compared to **DPQ**, but, on the other hand, it does not change much between **DPPN** and **H4PP**. All this clearly highlights the role of elongation of π-electron system in PP-based ligands, and in particular, upon its functionalization with helicene fragment, in inducing ILCT-type excitations (*vide infra*).

Regarding the complex (see Figure 2 top for (P,C_{Re})-**Re-H4PP**^{I} and the SI for (P,A_{Re})-**Re-H4PP**^{II}), its HOMO and LUMO reveal highly similar characteristics as that in the pristine ligand with some minimal contribution from the Re center observed for the HOMO orbital. Nonetheless, the Re d orbitals appear not to be strongly involved in the electronic π-system of the H4PP fragment. Importantly, however, both HOMO and LUMO are notably stabilized by the introduction of the metal center in **Re-H4PP** as compared to **H4PP**, with the effect being more pronounced for LUMO, which results in a decrease of the HOMO/LUMO gap for the complex *vs.* the ligand ($\Delta E_{HOMO/LUMO}$ = 5.846 eV *vs.* 6.035 eV). Additionally, reflecting the coordination of the metal to the phenanthroline nitrogen atoms, the π* orbital centered at this fragment undergoes an even more remarkable stabilization (see E_{orb} of LUMO+1 in Figure 2 and the SI), which, accompanied by a presence of high-energy occupied Re-centered MOs (see e.g. HOMO-1 in Figure 2 and HOMO-2 in the SI), may further increase importance of different CT contributions in determining the photophysical and chiroptical responses of the complex when compared with the ligand. Comparing the FMO orbitals of the Re(I)-helicene complex with those for the considered model systems, notable similarities between **Re-DPPN** and **Re-H4PP** can be observed, with both HOMO and LUMO being of ligand-centered character, and occupied MOs involving Re d orbitals appearing at higher energies. For **Re-DQP**, on the other hand, LUMO, centered mainly on the phenanthroline fragment, resembles rather LUMO+1 than LUMO of **Re-H4PP** and, more importantly, HOMO is localized at the metal fragment. This implies that the less extended π-electron system in the ligand increases importance of MLCT states in its Re complexes, while for π-elongated molecules, some interplay between MLCT, ILCT and ππ* states can be expected.

Table 1. Summarized photophysical properties of **H4PP** and **Re-H4PP** compared with non-helicene derivatives **DQP**, **DPPN**, **DPPZ**, **Re-DQP**, and **Re-DPPZ**. Measurements for **H4PP** and **Re-H4PP** were performed in dichloromethane at room temperature (298 K) and in frozen glassy matrix in 2-MeTHF at 77 K. 'n.r.' stands for 'not reported'. Chemical structures of **DPPN**, **Re-DQP**, **Re-DPPZ**, and **Re-H4PP** are provided below.

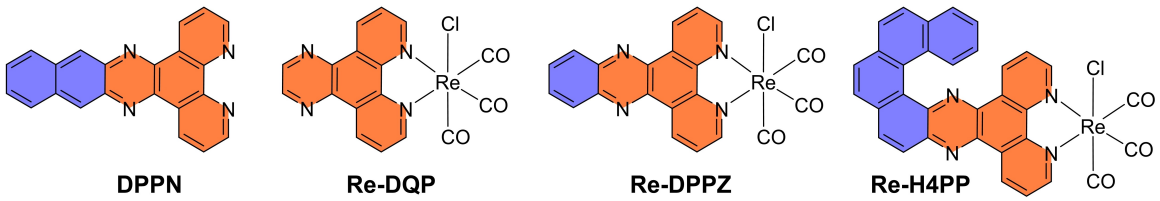

Compound	Absorption λ_{max}/nm (ε/10^4 $M^{-1}cm^{-1}$) (solvent)	Emission properties at 298 K[a]		
		λ_{max}/nm (solvent or *T*)	Φ_{lum} (CH_2Cl_2)	τ/ns (CH_2Cl_2)
DQP	230 (2.8), 251 (4.3), 278 (1.2), 299 (1.0), 324 (0.4) (CH_3CN)[14]	430 (DMF)[19] 419 (EtOH)[20]	n.r.	n.r.
DPPZ	270 (4.37), 367 (1.13), 379 (1.29) (CH_2Cl_2)[15a]	415 (CH_2Cl_2)[15b]	0.006	3000 (deaerated)
DPPN	316 (6.0), 372 & 391 & 413 (≤1.0)[b] (CH_2Cl_2)[16b]	550, 600 (CH_2Cl_2)[16b] 550 (CH_3CN)[16c]	n.r.	n.r.
H4PP	260 (8.5), 288 (6.7), 350 (3.3), 435 (1.3), 410 (1.6) (CH_2Cl_2)	515 (CH_2Cl_2) 560 (77 K)	0.29	5.8, 2.8
Re-DQP	257 (4.7), 291 (1.9), 380 (0.3) (CH_3CN)[14]	n.r.	n.r.	n.r.
Re-DPPZ	280 (5.00), 360 (1.38)[15a]	415 (CH_2Cl_2)[15b]	<0.0001	n.r.
Re-H4PP	267 (7.7), 304 (4.0), 353 (2.9), 460 (1.2) (CH_2Cl_2)	518 (CH_2Cl_2) 560 (77 K)	0.02	1.2, 7.6

[a] Note that aerated and deaerated measurements for **H4PP** and **Re-H4PP** gave similar results. [b] Exact values not reported.

Experimental Photophysical Properties

Absorption and emission spectra of **H4PP** were measured in CH_2Cl_2 at room temperature (298 K) and in 2-methyltetrahydrofuran (2-MeTHF) at low temperature (77 K); they are presented in Figure 3 and in Table 1. To highlight the impact of helicene backbone, these photophysical results were compared with those for the non-helicene analogues **DQP**, **DPPZ**, and **DPPN**. The absorption spectrum of **H4PP** reveals distinct features. In the higher-energy region a strong absorption band peaking at 260 nm (ε~85,000 $M^{-1}cm^{-1}$) along with a shoulder at 288 nm (ε = 67,100 $M^{-1}cm^{-1}$) were observed. Another pronounced band at 350 nm (ε = 33,000 $M^{-1}cm^{-1}$) with shoulders at 410 nm (ε = 16,500 $M^{-1}cm^{-1}$) and 435 nm (ε = 13,100 $M^{-1}cm^{-1}$) was evident, with the absorption tail extending up to 500 nm. For comparison, planar **DQP**[14] in acetonitrile and **DPPZ**[15] in dichloromethane display intense to moderate bands between 230 and 380 nm (see Table 1), thus showing that **H4PP** absorption spectrum is significantly red-shifted and has much higher molar absorptivity, which underscores the profound influence of the helicene backbone on the photophysical properties. Actually, **H4PP** compares well with planar and π-extended **DPPN**[16b] that has been reported to exhibit in dichloromethane distinct signals at 316 nm (of highest intensity, ε~60,000 $M^{-1}cm^{-1}$) and at 372, 391, 413 nm (ε ≤ 10,000 $M^{-1}cm^{-1}$) with a tail up to 502 nm.

The luminescence spectrum of **H4PP** exhibits a broad featureless profile in dichloromethane at ambient temperature, with a peak fluorescence wavelength ($\lambda_{max,Fl}$) at 515 nm. Importantly, a rather high photoluminescence quantum yield (PLQY) of 29% was obtained, significantly increased compared to not only the non-helicenic analogue **DPPZ** (for which PLQY is only 0.6%[15b]) but also helicene fused with other functional groups such as bipyridine[17] or thiadiazole,[9] marking advantageous cooperation of both units (both structural and electronic) in emission processes in **H4PP**. Low-energy absorption between 370 and 470 nm observed for **H4PP** suggests an involvement of charge-transfer states. The excitation spectrum of **H4PP** clearly confirms that such states are responsible for the room temperature luminescence (see Figure S1.6). This CT character is indicated by the broad featureless nature of the emission spectrum and is also confirmed by theoretical analysis (*vide infra*). Excited-state lifetime of **H4PP** was measured and accurately described by a two-component exponential decay function (Figure S1.4). The longer decay component exhibits a lifetime of 5.8 ns, contributing 36% to the overall decay process, whereas the faster decay component, contributing 64%, has a lifetime of 2.8 ns. At 77 K in 2-MeTHF, **H4PP** displays a peak phosphorescence wavelength ($\lambda_{max,Ph}$) at 560 nm, with a shoulder at 604 nm most probably due to vibronic progression. The calculated vibronic progression value around 1300 cm^{-1} is well-reported in helicene literature as arising from C=C or C=N stretching bands.[11,12] Energy difference between the ground state and the singlet excited state which emits at room temperature was calculated to be 2.70 eV. Similarly, energy difference between the ground state and the triplet excited state which emits at 77 K was determined to be 2.32 eV. The energy gap between these two excited states is 0.38 eV or 3000 cm^{-1}.

Upon coordination of rhenium(I) to the **H4PP** ligand, the resulting complex **Re-H4PP** exhibits very similar UV-Vis absorption in the higher-energy region as the ligand (Figure 4 and Table 1). The spectrum in CH_2Cl_2 displayed a strong absorption band centered at 267 nm (ε~77,450 $M^{-1}cm^{-1}$) accompanied by a shoulder at 304 nm (ε~40,100 $M^{-1}cm^{-1}$), a pronounced absorption band at 353 nm (ε~28,850 $M^{-1}cm^{-1}$) and a shoulder at 460 nm (ε~11,700 $M^{-1}cm^{-1}$). Under identical spectroscopic conditions, the tail of absorption spectrum for the Re(I) complex is notably red-shifted compared to the ligand reaching up to

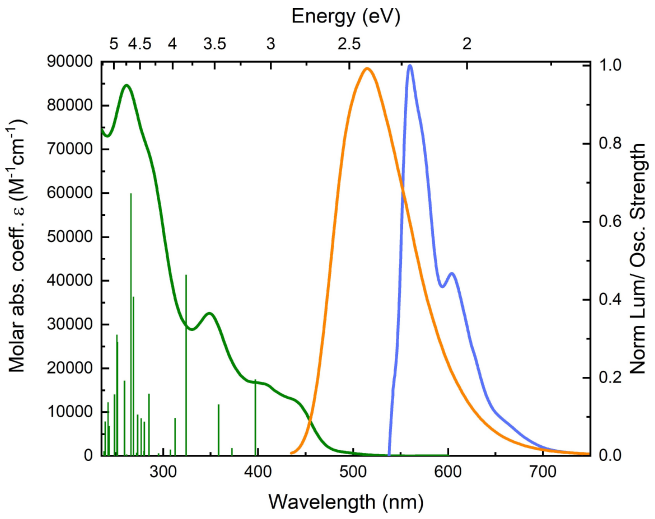

Figure 3. Absorption (green line) and normalized emission spectra in CH_2Cl_2 at 298 K (orange line) and in 2-MeTHF at 77 K (light blue line) of **H4PP**, *C* 1×10^{-5} M, excitation wavelength = 425 nm. Calculated (TDDFT-LC-PBE0*/def2-TZVP/PCM(CH_2Cl_2)) excitation energies along with the corresponding oscillator strengths indicated as green 'stick' spectrum.

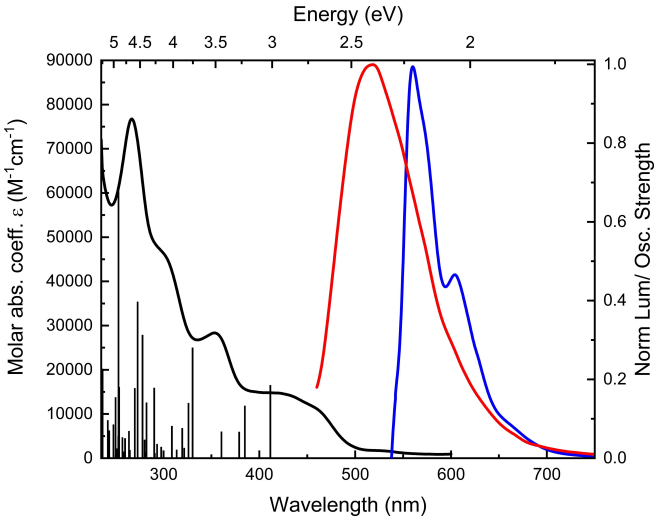

Figure 4. Absorption (black line) and normalized emission spectra in CH_2Cl_2 at 298 K (red line) and in 2-MeTHF at 77 K (dark blue line) of **Re-H4PP**, *C* 5×10^{-6} M, excitation wavelength = 425 nm. Calculated (TDDFT-LC-PBE0*/def2-TZVP/PCM(CH_2Cl_2)) excitation energies along with the corresponding oscillator strengths obtained for (P,C_{Re})-**Re-H4PP**^{I} indicated as black 'stick' spectrum.

575 nm (for a direct comparison, see Figure S1.7). The effect of the helicene moiety is clearly visible for example by comparing the absorption for **Re-H4PP** with the literature one for **Re-DQP** in acetonitrile, which, as expected, appears to be blue-shifted and of lower intensity *vs.* the helicenic complex (see Table 1).[14]

As for **H4PP**, the emission spectra of **Re-H4PP** were then recorded in CH_2Cl_2 at ambient conditions (298 K) and in 2-MeTHF at 77 K (see Figure 4). The emission properties of **Re-H4PP**, measured under similar conditions to those employed in the case of **H4PP**, remain largely influenced by the ligand scaffold, highlighting rather minimal impact of the metal center on the photophysical properties (for a direct comparison, see Figure S1.8). At room temperature, a featureless broad signal was observed, whereas at low temperature, a structured emission spectrum with vibronic substructure was obtained. Interestingly, the PLQY of **Re-H4PP** ($\Phi_f = 2\%$) is found one order of magnitude higher than for the previously reported mononuclear rhenium-bipyridine-helicene complexes (0.1–0.3 %)[11] but lower than for rhenium-NHC-helicene complexes (5–13 %).[12] It is also noteworthy that analogous non-helicene Re(I) complexes, such as for example **Re-DPPZ**, are rather weak emitters (i.e. PLQY $< 10^{-4}$).[15b] Similarly to **H4PP**, emission decay of **Re-H4PP** is found bi-exponential, with a faster lifetime component at 1.2 ns (accounting for 87 %) and a more extended lifetime component of 7.6 ns (representing 13 %), see Figure S1.5. The observed lifetime is much shorter than that reported for rhenium-bipyridine-helicene complexes, which typically ranges between 25 ns and 40 ns.[11] As can be noticed, while the lifetime value changes slightly, there is no significant alteration to the nature of radiative decay for **Re-H4PP** compared to the ligand. This could indicate that the emission predominantly originates from the ligand itself and the rhenium contribution is modest. Actually, as reported for the **DPPZ**-based $Re(CO)_3Cl$ complexes and confirmed here *via* quantum-chemical calculations (*vide infra*), the photophysics of such systems can be complicated, with, for example, the lowest-energy triplet excited state for **Re-DPPZ** being supposedly the intra-ligand $^3\pi\pi^*$ at 77 K and the ^{3}MLCT at 298 K.[18]

Experimental Chiroptical Properties (ECD and CPL Activity)

While the ligand could not be resolved into respective enantiomers, it was possible to obtain pure enantiomers for its Re(I) complex **Re-H4PP**. ECD and CPL studies were therefore conducted on these samples. Under ambient conditions in dichloromethane, the enantiomers of **Re-H4PP** exhibit mirror-image ECD spectra, as demonstrated in Figure 5. Specifically, the (*P*)-**Re-H4PP** enantiomer presents a positive ECD band at 540 nm with a molar ellipticity $\Delta\varepsilon = +13\ M^{-1}cm^{-1}$ and an additional, more pronounced peak at 408 nm ($\Delta\varepsilon = +71\ M^{-1}cm^{-1}$). In the higher-energy region, a notable peak at 311 nm ($\Delta\varepsilon = +98\ M^{-1}cm^{-1}$) is followed by an inversion in the ECD signal, exhibiting a pronounced negative peak at 243 nm ($\Delta\varepsilon = -106\ M^{-1}cm^{-1}$). The (*P*) and (*M*) assignments were based on theoretical calculations (*vide infra*).

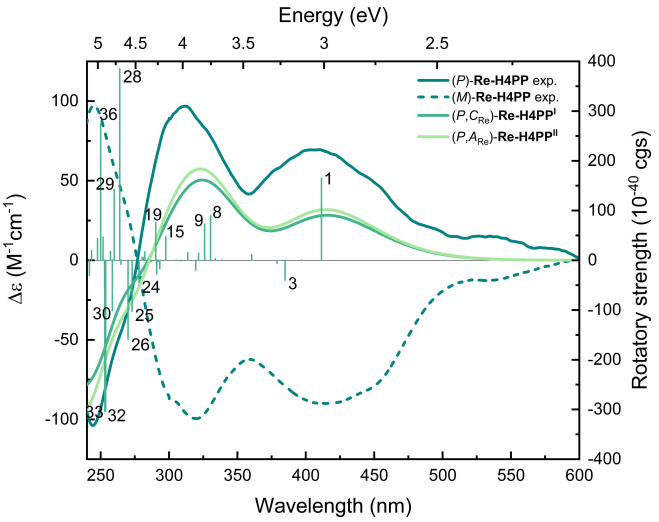

Figure 5. ECD spectra of **Re-H4PP** in dichloromethane at 298 K (blue-green solid/dash line for (*P*)/(*M*) enantiomer), *C* 2×10^{-5} M, along with the corresponding simulated (TDDFT-LC-PBE0*/def2-TZVP/PCM(CH_2Cl_2)) spectral envelopes obtained for (P,C_{Re})-**Re-H4PP**^{I} and (P,A_{Re})-**Re-H4PP**^{II} (dark green and light green lines, respectively). Selected numbered excitation energies and the corresponding rotatory strengths obtained for (P,C_{Re})-**Re-H4PP**^{I} indicated as 'stick' spectrum correspond to those analyzed in detail (see the SI).

In line with the ECD spectra, both the (*P*) and (*M*) enantiomers of **Re-H4PP** demonstrated CPL signals both at ambient temperature in dichloromethane and at 77 K in 2-MeTHF, as illustrated in Figure 6. The CPL signals at room temperature correlated with the ECD signals; specifically, the (*P*)-**Re-H4PP** showed a positive CPL response, with the measured g_{lum} value of $+2.3\times10^{-3}$ at 507 nm. Notably, the CPL signal was amplified at the cryogenic temperature of 77 K, alongside a more pronounced vibrational progression. At this lower temperature, the g_{lum} values were observed to peak at $+2.9\times10^{-2}$ at 560 nm, indicating enhanced chiroptical behavior. It is worth noting that the magnitude of g_{lum} exhibits negligible variation

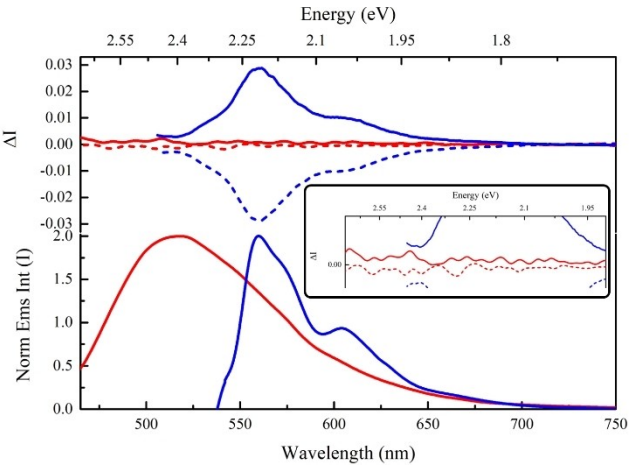

Figure 6. Photoluminescence spectra of **Re-H4PP** in dichloromethane at 298 K (red line) and in 2-MeTHF at 77 K (blue line), *C* 2×10^{-5} M. Spectra for (*P*) and (*M*) enantiomers of **Re-H4PP** are represented by solid and dashed lines, respectively. Inset: Enlarged 298 K spectra.

at 77 K, where the vibronic progression of the T_1 excited state introduces slight fluctuations in the g_{lum} values (Figure 7). This pattern strongly infers that the chiroptical response remains relatively stable due to a single excited state predominantly influencing the system with minimal deviation. Conversely, at ambient temperature, the dynamics of the system become more complex, as indicated by the presence of bi-exponential decay. The participation of various electronic excited states, along with their vibronic sublevels, plays a significant role in the radiative processes, leading to variations in the g_{lum} values at 298 K. Nonetheless, the consistency in the sign across the emission spectrum points to a certain degree of uniformity within these excited states.

Computational Analysis of Photophysical and Chiroptical Properties

The UV-Vis absorption spectra of the ligand **H4PP** and its Re(I) complex **Re-H4PP** calculated at the TDDFT-LC-PBE0*/def2-TZVP/PCM(CH_2Cl_2) level of theory agree fairly well with the measured ones, except for a slight blue-shift, particularly visible in the lower-energy region (see Figures 3 and 4, and Figure S2.2). Nonetheless, the derived IP-tuned LC-PBE0* functional (see Computational details in the SI) correctly reproduces, in a satisfactory manner, both the measured spectral envelopes and the visible red-shift with the increase in intensity of the low-energy tail observed experimentally for the Re(I) complex *vs.* the ligand. Note that both considered diastereomers, (P,C_{Re})-**Re-H4PP^{I}** and (P,A_{Re})-**Re-H4PP^{II}**, show practically the same computed absorption spectra. A good agreement of the absorption computations with the experimental data was also obtained for the model (non-helicene) systems: **DQP** and **Re-DQP**, considering the spectra measured in acetonitrile[14] and **DPPN**, as compared with the data obtained in dichloromethane[16b] (Figure S2.6). Some visible deviations from the experiments correspond to a slight blue-shift of the computed intensity in the higher-energy region and, for **DQP** and **DPPN** (for which not only the measured absorption maxima but also the whole spectra were found in the literature),[14,16b] to a more structured shape of the experimental spectral envelopes in the lower-energy region, at *ca.* 270–350 nm and *ca.* 370–425 nm, respectively, which may be indicative of the vibronic nature of these absorption bands. Importantly, the performance of the IP-tuned LC-PBE0* functional appears to be also advantageous for the simulation of **Re-H4PP** ECD spectrum (see Figure 5 and Figure S2.3), considering both the shape of the spectral envelopes and energetic position of the main maxima. Some deviations from the experiment regards the absence of an extended intensity in visible region, which may be connected to generally underestimated intensity of the computed spectrum, an overestimation of the energy of the lowest-energy excitations and/or disregard of vibronic effects in the corresponding ECD calculations. The positive/negative sign of ECD intensity at wavelengths longer/shorter than 285 nm observed in the simulated ECD spectra of (P,C_{Re})-**Re-H4PP^{I}** and (P,A_{Re})-**Re-H4PP^{II}** (fully corresponding to the experimental data obtained for (*P*)-**Re-H4PP**) allowed for a decisive assignment of (*P*) and (*M*) helical configuration. Note that since the ECD as well as UV-Vis spectral envelopes computed for two **Re-H4PP** diastereomers hardly differ, one cannot ascertain based on the calculations whether either one or the other or a mixture of both can be actually present during the measurements.

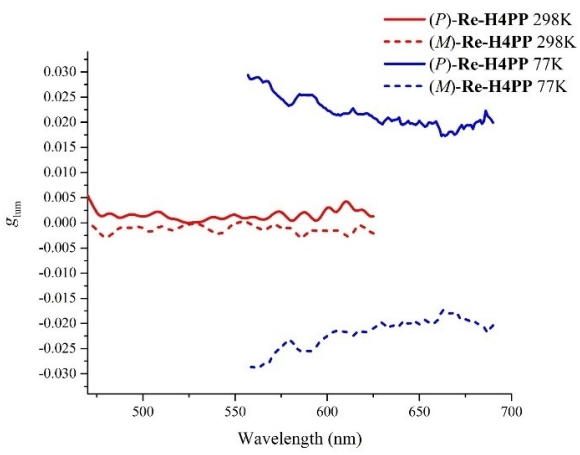

Figure 7. g_{lum} spectra of **Re-H4PP** in dichloromethane at 298 K (red line) and in 2-MeTHF at 77 K (blue line), *C* 2×10^{-5} M. Spectra for (*P*) and (*M*) enantiomers of **Re-H4PP** are represented by solid and dashed lines, respectively.

An analysis of underlying dominant excitations in terms of MO-pair contributions was then performed to assign particular bands and rationalize the observed spectroscopic trends (see the SI: Tables S2.2–4, Figures S2.4–5 and S2.9–11 for the helicene-based systems; Tables S2.5–8 and Figures S2.7–8 and S2.12–15 for the considered models). Based on the presented computed results, the low-energy UV-Vis absorption intensity measured for the **H4PP** ligand (the shoulder centered at 435 nm) originates mainly from the lowest-energy excitation no. 1, calculated at 397 nm, which corresponds to HOMO→LUMO (dominant) and HOMO-1→LUMO transitions, jointly representing ILCT from the helicene core to the pyrazino-phenanthroline moiety, mixed with some ππ* component localized at the pyrazine and adjacent helicene's rings (see Figure 2, Table S2.2 and Figure S2.9). The higher-energy intensity centered at 350 nm in the experimental spectrum appears to be due to excitations nos. 3, 4 and 5 (computed at 358, 324 and 313 nm, respectively) that show a ππ* and [4]helicene→pyrazine-phenanthroline ILCT character, mixed, exclusively for no. 3, with a formally forbidden nπ* contribution with non-bonding orbitals representing the lone-pairs (LPs) of the pyrazine and phenanthroline nitrogen atoms. Note that the ππ* component in these excitations is either delocalized across the whole molecular structure (nos. 3 and 5) or centered at [4]helicene-pyrazine (no. 4). The higher-energy excitations that underlie third absorption peak recorded at 260 nm (such as for example nos. 15 and 16 with sizable oscillator strength values, Table S2.2) also show combined ππ*/ILCT nature. In this spectral region, additional admixture of pyrazine-/phenanthroline-origin nπ* transitions is also generally observed (e.g. nos. 19 and 26).

The effect of the extension of the π-electron system and the accompanied polarization of the HOMO/LUMO electron density (see Figure 2) on UV-Vis absorption in pyrazino-phenanthroline derivatives becomes apparent from the comparative analysis of the simulated spectra and the nature of the underlying electronic transitions for the studied helicene-based and non-helicenic model systems. Namely, as seen in the experiments (*vide supra*) and reproduced here by the calculations (see Figure S2.6), the lowest-energy UV-Vis absorption intensity red-shifts with an extension of π-electron system fused with pyrazino-phenanthroline moiety, that is across the series of **DQP** (the shortest wavelength, no additional aromatic rings) < **DPPN** (naphthalene) < **H4PP** (the longest wavelength, [4]helicene), with the most tremendous difference observed between **DQP** and **DPPN**. In the considered spectral range, the simulated spectrum of **DQP** comprises a peak at *ca.* 240 nm with a shoulder extending up to *ca.* 345 nm, whereas for **DPPN** three absorption bands, positioned at *ca.* 230, 300, and 360 nm, are observed, with the lowest-energy one characterized by a tail up to *ca.* 500 nm, quite similar to that observed for **H4PP**. The first absorption band for **DQP** arises predominantly from the excitations nos. 7, 11 and 12, while its shoulder from the excitation no. 2 corresponding to HOMO→LUMO transition (see Figure S2.7). These excitations demonstrate ππ* character (within π-electron system delocalized over the whole molecule) with a minor phenanthroline→pyrazine/pyrazine→phenanthroline ILCT signatures (see Table S2.5 and Figure S2.12, and also Figure 2). Excitations nos. 3 and 6 (HOMO-1→LUMO and HOMO→LUMO + 2) of **DPPN**, which give rise to bands at *ca.* 360 and 300 nm, respectively, and excitation no. 1 (HOMO→LUMO), which has a low oscillator strength and contributes to the observed absorption tail, show the increased ILCT (pyrazino-naphthalene→phenanthroline) component to the ππ*-type transitions involving π-electron system enlarged compared to **DQP** (see Figure S2.8, Table S2.6 and Figure S2.13, and also Figure 2), which may account for the spectral differences between **DPPN** and **DQP**, and similarities between **DPPN** and **H4PP**. As detailed above, helicenic functionalization enhances further the ILCT contribution that combined with more delocalized character of ππ* transitions lead to more extended absorption in the visible region observed for **H4PP** *vs.* **DPPN** (and **DQP**).

As elaborated in the experimental section, while **Re-H4PP** exhibits fairly similar UV-Vis absorption pattern to that of **H4PP**, the incorporation of the metal center into the helicenic pyrazino-phenanthroline framework nevertheless has some influence on the photophysical features of the resulting complex as compared to the ligand, particularly in the low-energy region of the spectrum, which is also visible in the computed results (see Figure S2.2). Notably, the lowest-energy excitation computed for **Re-H4PP** (no. 1) has essentially the same oscillator strength value (and consequently intensity) as that of **H4PP** and demonstrates similar electronic characteristics corresponding to almost pure HOMO→LUMO [4]helicene→pyrazino-phenanthroline ILCT transition with some helicene-centered ππ* signature but with additional MLCT component due to involvement of Re orbital (compare Table S2.2 and Figure S2.9 with Tables S2.3–4 and Figures S2.10–11, see Figure 2). This excitation appears however at lower-energy (longer-wavelength) value (411 nm) than for **H4PP** (397 nm), reflecting the aforementioned decrease in the HOMO/LUMO gap observed for the complex *vs.* the ligand due to a pronounced energetic stabilization of LUMO occurring upon complexation, which may explain the red-shift of the tail of absorption spectrum observed for **Re-H4PP** as compared to **H4PP**. Another excitation underlying the first absorption band is an excitation no. 3 computed at 385 nm, which involves HOMO-2→LUMO and HOMO-3→LUMO transitions corresponding to MLCT, ligand-to-ligand CT (LLCT, predominantly chloride→pyrazino-phenanthroline) and some helicene-centered ππ* (see Tables S2.3–4 and Figures S2.10–11). Importantly, these low-energy excitations were also calculated to be ECD-active, showing respectively positive (no. 1) and negative (no. 3) rotatory strength value for (*P*)-**Re-H4PP** independent of the chirality-at-rhenium configuration (see Figures 5 and Figure S2.5), with the former clearly dominating and giving rise to the first (lowest-energy) ECD band. Based on the performed simulations, the UV-Vis intensity measured for the complex at *ca.* 350 nm is due to two excitations with sizable oscillator strength values, no. 8 (computed at 330 nm) and no. 9 (326 nm), which both show [4]helicene→pyrazino-phenanthroline ILCT and ππ* (within π-electron system delocalized over [4]helicene and pyrazino-[4]helicene, respectively) character admixed with $Re(CO)_3Cl$→pyrazino-phenanthroline MLCT and LLCT (see Tables S2.3–4 and Figures S2.10–11). The excitations nos. 8 and 9 also afford substantial positive rotatory strength values and thus can be assigned as responsible for the second positive ECD band in the experimental spectrum of (*P*)-**Re-H4PP**. Higher-energy excitations accountable for the third absorption peak (centered at 267 nm in the experimental spectrum) are also an admixture of H4PP-localized ππ* and ILCT transitions accompanied by MLCT and chloride-CO→pyrazino-phenanthroline LLCT but with some $n(LP(N_{pyrazine}))\pi^*$ contributions (see for example nos. 24 and 25 computed at 278 and 273 nm, respectively). Finally, we would like to note in passing that the ECD spectrum simulated for (*P*)-**H4PP** shows overall similar features compared to that for (*P*)-**Re-H4PP** with two distinct bands of positive intensity computed between *ca.* 280 and 475 nm but on the other hand differs from (*P*)-**Re-H4PP**, for example, in the bands intensity and the position of the first (lowest-energy) maximum (see Figure S2.5). This clearly demonstrates further the important role of the Re(I) fragment and interplay between ligand-centered ILCT/ππ* and MLCT/LLCT transitions in determining the ECD spectral envelopes for the complex.

By comparing the shape of the first (lowest-energy) UV-Vis absorption band and extent of its tail in the simulated spectra for the studied helicene-based and model Re(I) systems, it can be concluded that helicenic functionalization of the pyrazino-phenanthroline appears to have a less prominent influence on the UV-Vis characteristics of the complex to that established for the ligand. Indeed, the first absorption peak computed for **Re-DQP** and **Re-DPPN** is positioned at comparable spectral range to that for **Re-H4PP**, showing expected blue-shift with a

decreasing extent of π-electron system of the ligand, and, for **Re-DPPN**, it additionally exhibits highly similar shape. The less notable effect of the helicene functionalization on the UV-Vis absorption of the complexes appears to be connected with new probable low-energy channels for the CT transitions induced upon coordination to the Re(I) center: MLCT and LLCT, which are indeed similarly utilized in both model and the helicene-based Re(I) complexes. Notably, for **Re-DQP**, the lower-energy band arises from the excitation no. 2, which corresponds to HOMO-1→LUMO of combined rhenium&chloride-CO→phenanthroline MLCT&LLCT character (see Figure S2.7, Table S2.7 and Figure S2.14, and also Figure 2). For **Re-DPPN**, the fist band stems from the excitation no. 3, while excitation no. 1 of low intensity contributes to the absorption tail (similarly to **DPPN**); see Figure S2.8. Excitation no. 1 corresponds to the HOMO→LUMO transition that can be assigned as ππ* with pyrazino-naphthalene→phenanthroline ILCT contribution, whereas excitation no. 3 involves HOMO-2→LUMO+1 and HOMO-2→LUMO of combined rhenium&chloride-CO→DPPN,phenanthroline MLCT&LLCT character (see Table S2.8 and Figure S2.15, and Figure 2), thus collectively corresponding well to the assignment of the low-energy absorption in **Re-H4PP**, which explains spectral similarities between these two compounds. Accordingly, it can be also noted that the decrease in intensity observed for the lowest-energy absorption band for **Re-DQP**, as compared to **Re-DPPN** and **Re-H4PP**, may be traced back to a lack of ligand-centered contributions.

The above presented computational analyses of the absorption properties of the ligand **H4PP** and its complex **Re-H4PP** indicate that the emitting S_1 excited state might be of similar characteristics for both the species, in line with their almost the same fluorescence spectra (Figure S1.8). To gain additional insight into luminescence features of these compounds, subsequent theoretical studies were performed involving S_1 and T_1 geometry optimizations at the (TDA−)TDDFT-LC-ωPBEh/def2-TZVP/CPCM(CH_2Cl_2) level of theory followed by the calculations of emission characteristics employing (TDA−)TDDFT-LCY-PBE0*/TZP/COSMO(CH_2Cl_2) with spin-orbit coupling (SOC).[21] For a complete description of the employed computational details and a full set of calculated data (Tables S2.9–13, Figures S2.16–24), see the SI.

The obtained S_1 and T_1 excited-state structures are presented in Figures S2.16 and S2.17, respectively. As can be seen, except for S_1-**H4PP**, despite the rigidity of the systems, the S_1 and T_1 geometry optimizations using different initial structures (see Computational details in the SI), yielded different stable minima on the corresponding excited-state potential energy surfaces. These conformers, distinguished by '**a**' and '**b**' superscripts, vary slightly in the geometry of the helicene unit (including, for example, changes in a helical pitch, particularly visible for S_1-**Re-H4PP**) and of the metal-based fragment (involving some shifts in the positions of CO and Cl ligands within the Cl–Re-CO axis). Note that, as for absorption, the corresponding diastereoisomers of (*P*,C_{Re})-**Re-H4PP^{I}** and (*P*,A_{Re})-**ReH4PP^{II}** demonstrate highly similar fluorescence and phosphorescence emission (see Table S2.9).

The computed vertical fluorescence wavelength values agree with the positions of measured maxima in rather satisfactory manner, 482 nm *vs.* λ_{exp} = 515 nm for S_1-**H4PP** and 519/543 nm *vs.* λ_{exp} = 518 nm for S_1-**Re-H4PP^{a}**/S_1-**Re-H4PP^{b}**, although, as can be seen, the calculations visibly overestimate experimental energetic difference in the fluorescence of the ligand and its complex. As expected, the $S_1 \rightarrow S_0$ emission transition in **H4PP** (involving predominantly HOMO and LUMO, see Figure S2.18) shows similar character to the $S_0 \rightarrow S_1$ absorption, that is mixed ^{1}ILCT (pyrazino-phenanthroline→[4]-helicene)/$^1\pi\pi^*$ (with π-electron density delocalized over pyrazine and the adjacent helicene rings). The fluorescence lifetime of *ca.* 11 ns obtained for S_1-**H4PP** agrees reasonably well with the experimental value of 5.8 ns derived from the two-component exponential decay model; two distinct fluorescence lifetimes observed experimentally for the ligand may be indicative of its higher conformational flexibility at 298 K than determined *via* the performed calculations. The S_1-**Re-H4PP^{a}** states demonstrate the same ligand-centered character as S_1-**H4PP**, which is also comparable to the $S_0 \rightarrow S_1$ absorption transition in **Re-H4PP**, but without slight contribution from the Re(I) center (*vide supra*). Conversely, S_1-**Re-H4PP^{b}** involving Re-fragment-centered HOMO and predominantly pyrazino-phenanthroline-centered LUMO and LUMO+1 corresponds accordingly to ^{1}MLCT/^{1}LLCT and, unlike S_1-**Re-H4PP^{a}**, is not fluorescent showing practically zero oscillator strength values. This may indicate its negligible role in determining fluorescence intensity for **Re-H4PP**, highlighted further by a visible discrepancy of its computed emission energy *vs.* the experiment and also a larger deviation from the calculated emission energy for the ligand. In line with different nature of $S_1 \rightarrow S_0$ emission transition in S_1-**Re-H4PP^{a}** and S_1-**Re-H4PP^{b}**, the computations yield different fluorescence lifetimes: *ca.* 20 and 1500 ns, respectively, both visibly overestimated with respect to the experiment (τ_{exp} = 1.2 ns and 7.6 ns), particularly for **Re-H4PP^{b}**. While similar electronic characteristics of the computed S_1-**H4PP** and fluorescent S_1-**Re-H4PP^{a}** may account for the similar fluorescence signals recorded for the ligand **H4PP** and its complex **Re-H4PP**, coexistence of S_1-**Re-H4PP^{a}** and S_1-**Re-H4PP^{b}** may explain two distinct fluorescence lifetimes and low (in comparison with **H4PP**) fluorescence quantum yield observed experimentally for **Re-H4PP** (*vide infra*). Finally, the emissive S_1-**Re-H4PP^{a}** structures show high rotatory strengths and their corresponding computed luminescence dissymmetry factor g_{lum} values have the same sign (positive for (*P*,C_{Re})-**Re-H4PP^{I}** and (*P*,A_{Re})-**Re-H4PP^{II}**) and order of magnitude as the experimentally measured ones (Table S2.9); note that the results of the performed calculations indicate that the **H4PP** ligand may also be CPL-active.

As far as the phosphorescence emission is concerned, the $T_1 \rightarrow S_0$ wavelengths computed for both **H4PP** and **Re-H4PP** are visibly red-shifted with respect to the experimental value of 560 nm, by 61/36 nm for **H4PP^{a}**/**H4PP^{c}**, and *ca.* 75/31/40 nm for **Re-H4PP^{a}**/**Re-H4PP^{b}**/**Re-H4PP^{c}**. We note in passing that the similar phosphorescence energies, in line with the measured data, were obtained for T_1-**H4PP^{c}** and '**a**' and '**b**' conformers of T_1-**Re-H4PP**. The $T_1 \rightarrow S_0$ transitions in T_1-**H4PP^{a}** and T_1-**H4PP^{c}** show the akin electronic character, LUMO→HOMO mixed ^{3}ILCT/$^3\pi\pi^*$, to that observed for $S_1 \rightarrow S_0$ in S_1-**H4PP**, with the former (T_1-**H4PP^{a}**) presumably demonstrating slightly increased ^{3}ILCT *via* additional LUMO→HOMO-2 contribution (Table S2.9 and Figure S2.19). As in the case of fluorescence emission, the computations indicate CPL activity of

the ligand also in T_1 excited state, although its sign cannot be easily predicted, as for T_1-**H4PP**^{a}/T_1-**H4PP**^{c} ((*P*) enantiomer) negative/positive g_{lum} value was simulated, the latter visibly corresponding to that computed for S_1-**H4PP**, reflecting the more alike electronic nature of both states. The T_1-**Re-H4PP**^{a} and T_1-**Re-H4PP**^{c} excited states also represent (predominantly LUMO→HOMO) ^{3}ILCT/$^3\pi\pi^*$ but mixed with (LUMO→HOMO-4) ^{3}MLCT arising from the involvement of Re(I) orbital in HOMO-4, accompanied additionally by some helicene-pyrazino-phenanthroline→CO ^{3}LLCT component in the case of T_1-(*P*,A_{Re})-**Re-H4PP**^{IIc}; the noteworthy exception is T_1-(*P*,C_{Re})-**Re-H4PP**^{Ic} that appears to be purely helicene-pyrazino-phenantroline-ligand-centered. In line with similar molecular structures of S_1- and T_1-**Re-H4PP**^{b}, the T_1→S_0 emission in T_1-**Re-H4PP**^{b} (involving LUMO→HOMO, LUMO+1→HOMO) originates from helicene-pyrazino-phenanthroline→$Re(CO)_3Cl$ ^{3}MLCT/^{3}LLCT. Interestingly, the g_{lum} values calculated for T_1-**Re-H4PP** structures have negative sign and are of order of 10^{-3} (or 10^{-2} for T_1-(*P*,A_{Re})-**Re-H4PP**^{IIa}) except for T_1-(*P*,C_{Re})-**Re-H4PP**^{Ib}, which in line with the experiment ($g_{lum,exp}=2.9\times10^{-2}$ for (*P*)-**Re-H4PP**) is positive, although underestimated, 1.1×10^{-3}. Note that the opposite sign g_{lum} values obtained for T_1-(*P*,C_{Re})-**Re-H4PP**^{Ib} (positive) and T_1-(*P*,A_{Re})-**Re-H4PP**^{IIb} (negative), both showing similar ^{3}MLCT/^{3}LLCT character without pyrazino-phenanthroline-helicene-centered ILCT/$\pi\pi^*$ contributions, appear to reflect their different chirality-at-metal configurations. Based on this, it can be cautiously tentatively suggested that (*P*,C_{Re})-**Re-H4PP**^{Ib} may be responsible for the circularly polarized phosphorescence signal measured at 77 K. Further studies are however needed to verify reliability of the obtained TDA−TDDFT results and accordingly the importance of this structure in determining experimental phosphorescence for the complex in question, especially as it is known that the Tamm-Dancoff approximation to TDDFT (see Computational details in the SI) may misrepresent a value and/or sign of weak rotatory strengths, as those observed here. For example, we noticed that while for T_1-(*P*)-**Re-H4PP**^{a} rotatory strengths for all three triplet components computed with SOC are negative, in the case of T_1-(*P*)-**Re-H4PP**^{c} one appears always positive but it is overpowered by remaining negative components in the computed g_{lum} values.

Finally, a possible ISC pathway resulting in population of the lowest triplet excited state in the ligand **H4PP** and its complex **Re-H4PP** was investigated by analyzing computed singlet-triplet energy gap and corresponding spin-orbit coupling strength values along with electronic character of SOC-coupled states (see Tables S2.10–S2.13 and Figures S2.20–S2.24, and Figure 8). The calculations performed at S_1-**H4PP** and S_1-**Re-H4PP**^{a} structures predict the presence of four triplet excited states of energy below (T_1 and T_2) or closely above (T_3 and T_4) to that of S_1, with the lowest-energy gap and simultaneously the highest SOC interaction obtained in each case for S_1/T_2 ($\Delta E_{S1\text{-}T2}$ of 0.14 eV for the ligand and of 0.03–0.06 eV for the complex; SOC of *ca.* 5 cm^{-1}, which appears to be a typical value for phosphorescent organic helicene-based compounds).[22] Accordingly, the transition to the triplet manifold should most probably occur *via* S_1→T_2 ISC channel with both states involving an admixture of pyrazino-phenanthroline-helicene-centered ILCT/$\pi\pi^*$, but for T_2-**H4PP** of presumably larger ILCT contribution and for T_2-**Re-H4PP**^{a} with some MLCT/LLCT signature as indicated by the canonical MOs in Figure S2.21. As the SOC sizably mixes T_2 and T_1 and then T_1 with S_0 (see Table S2.10), after S_1→T_2 ISC, the T_2→T_1 internal conversion (IC) is expected, followed by T_1→S_0 phosphorescence emission (Figure 8). While for the ligand this appears the only possible phosphorescence mechanism, the computational analysis shows that in the case of **Re-H4PP** much more efficient ISC process can occur involving non-fluorescent S_1-**Re-H4PP**^{b}, demonstrating tremendously increased SOC interaction values relative to those aforementioned for S_1-**Re-H4PP**^{a}, *ca.* 700 cm^{-1}, between the S_1 and T_2 triplet states, again characterized by the lowest-energy gap ($\Delta E_{S1\text{-}T2}$ of *ca.* 0.1 eV for both diastereomers). Both S_1-**Re-H4PP**^{b} and T_2-**Re-H4PP**^{b} show pure MLCT/LLCT (predominantly pyrazino-phenanthroline→$Re(CO)_3Cl$) character without $\pi\pi^*$/ILCT contributions localized at the helicenic ligand but with different Re(I)-centered antibonding orbital involved (see Figure 8), resulting in strong SOC following the so-called 'organometallics version of El-Sayed's rule'.[21c] Note that when the same Re(I)-centered orbital is involved, as for S_1-**Re-H4PP**^{b} and T_1-**Re-H4PP**^{b}, indeed much lower SOC values were obtained, close to those for **Re-H4PP**^{a}. Further analysis of spin-orbit interactions between T_1, T_2, and S_0 at **Re-H4PP**^{b} again predicts T_2→T_1 IC and T_1→S_0 emission, which seems to cautiously support further the assignment of the experimentally observed phosphorescence/CPL emission to the T_1-**Re-H4PP**^{b} structure.

Conclusions

In the presented work, we described the preparation of the first helical pyrazino-phenanthroline PP ligand, namely [4]helicene-pyrazino[2,3-*f*][1,10]phenanthroline **H4PP** and its corresponding $Re(CO)_3Cl$ complex **Re-H4PP**. Through absorption and emission spectroscopy at room and low temperatures along with lifetime measurements and quantum-chemical modelling, we probed the corresponding low-lying excited states, showing interesting interplay between H4PP-centered ILCT and $\pi\pi^*$ and metal-fragment-involved MLCT and LLCT.

The reported herein coordination motif demonstrated similar σ-donating characteristics to that observed for bipyridine systems[11] but with enhanced structural rigidity. The latter combined with the ILCT/$\pi\pi^*$ character of the emitting excited state allow this novel coordination motif to have much brighter photoluminescence compared not only to non-helicene analogues such as **DPPZ** but also to analogous helicene-bipyridine or helicene-thiadiazole derivatives.[9,17] Upon integration of the Re(I) center, the PLQY stays one order of magnitude higher than for similar helicene-bipyridine complexes and much higher than weakly emitting non-helicene analogues, e.g. **Re-DPPZ**. Apart from the efficient fluorescence, both systems exhibited also low-temperature phosphorescence, which was studied herein for the first time for Re(I) complexes.

Additionally, enantioenriched samples containing the rhenium(I) metal center were prepared, allowing for the detailed study on chirality associated with the observed CT/$\pi\pi^*$ transitions. Notably, chiroptical activity was observed in the lower-energy bands, as evidenced in ECD and CPL both at room temperature and at 77 K, constituting thus the first study of CPL phosphor-

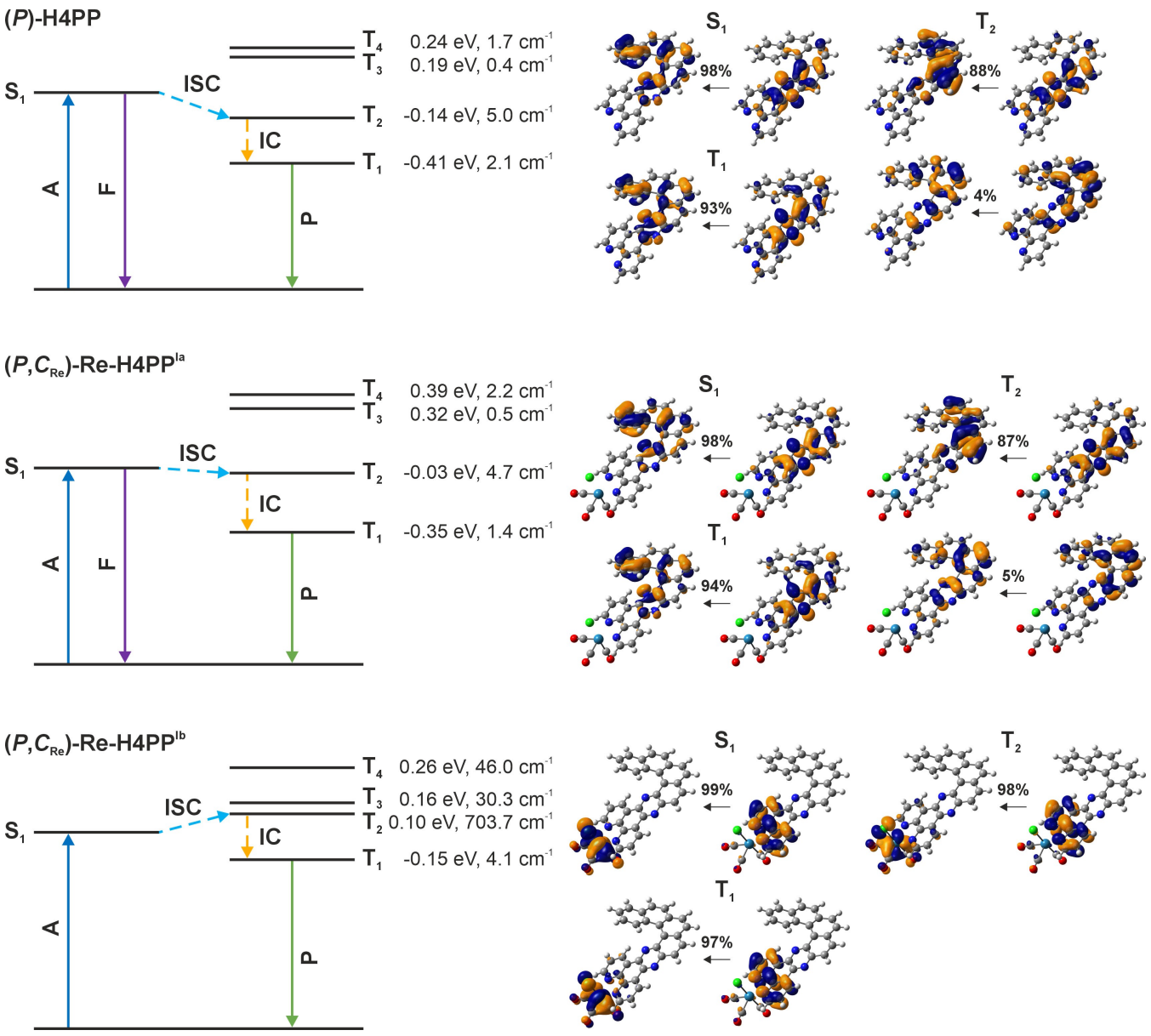

Figure 8. Schematic representation of photophysical processes in the ligand **H4PP** and its Re(I) complex **Re-H4PP** along with isosurfaces (±0.04 au) of natural transition orbital pairs for electronic transitions in the analyzed excited states. A – absorption, F – fluorescence, P – phosphorescence, ISC – intersystem crossing, IC – internal conversion. Numbers listed are S_1/T_n energy gaps ($\Delta E_{Tn\text{-}S1}$ in eV) and the corresponding SOC magnitudes (in cm^{-1}). Based on TDA–TDDFT calculations with spin-orbit coupling.

escence at low temperature in rhenium complexes. The corresponding anisotropy factor g_{lum} of 2×10^{-3} was found in dichloromethane at room temperature, and it increased to *ca.* 10^{-2} in a frozen glassy matrix at 77 K, establishing one of the highest g_{lum} reported till date for Re(I) systems.

By marrying the intricate interplay between PP features, novel architectural design and metal coordination, we thus unveiled a new type of helicene rhenium(I) complex and study the fundamental chemistry governing its photophysics by a blend of experimental data and theoretical computations. The presented results not only deepen our understanding of the structural and electronic complexities of helicene-based rhenium(I) systems but also pave the way for future innovations in asymmetric photoredox catalysis and CPL-active materials.

Acknowledgements

We acknowledge the Ministère de l'Education Nationale, de la Recherche et de la Technologie, the Centre National de la Recherche Scientifique (CNRS), Rennes Métropole and the French National Agency (ANR, LumoMat-E project, 18-EURE-0012). The European Commission Research Executive Agency (Grant Agreement number: 859752 — HEL4CHIROLED — H2020-MSCA-ITN-2019) is thanked for financial support. M.S.-H. and

D.J. gratefully acknowledge Polish high-performance computing infrastructure PLGrid (HPC Centers: ACK Cyfronet AGH, WCSS, CI TASK) for providing computer facilities and support within computational grants nos. PLG/2023/016764 and PLG/2024/017254. The computational study was carried out in part using research infrastructure funded by the European Union in the framework of the Smart Growth Operational Programme, Measure 4.2; Grant No. POIR.04.02.00-00-D001/20, "ATOMIN 2.0 – Center for materials research on ATOMic scale for the INnovative economy".

Conflict of Interests

The authors declare no conflict of interest.

Data Availability Statement

The data that support the findings of this study are available in the supplementary material of this article.

Keywords: Helicene · Rhenium · Dppz · CPL · Theoretical calculations

[1] Selected examples:a) B. Elias, C. Creely, G. W. Doorley, M. M. Feeney, C. Moucheron, A. Kirsch-DeMesmaeker, J. Dyer, D. C. Grills, M. W. George, P. Matousek, A. W. Parker, M. Towrie, J. M. Kelly, *Chem. Eur. J.* **2008**, *14*, 369–375; b) P. M. Keane, F. E. Poynton, J. P. Hall, I. V. Sazanovich, M. Towrie, T. Gunnlaugsson, S. J. Quinn, C. J. Cardin, J. M. Kelly, *Angew. Chem. Int. Ed.* **2015**, *54*, 8364–8368; c) C. J. Cardin, J. M. Kelly, S. J. Quinn, *Chem. Sci.* **2017**, *8*, 4705–4723; d) C. Yang, Q. Zhou, Z. Jiao, H. Zhao, C.-H. Huang, B.-Z. Zhu, H. Su, *Commun. Chem.* **2021**, *4*, 68; e) Q. Deraedt, L. Marcélis, F. Loiseau, B. Elias, *Inorg. Chem. Front.* **2017**, *4*, 91–103; f) M. Stitch, R. Sanders, I. V. Sazanovich, M. Towrie, S. W. Botchway, S. J. Quinn, *J. Phys. Chem. B* **2024**, *128*, 7803–7812.

[2] Selected examples: a) H. D. Stoeffler, N. B. Thornton, S. L. Temkin, K. S. Schanze, *J. Am. Chem. Soc.* **1995**, *117*, 7119–7128; b) V. Wing-Wah Yam, K. Kam-Wing Lo, K.-K. Cheung, R. Yuen-Chong Kong, *J. Chem. Soc., Dalton Trans.* **1997**, 2067–2072; c) G. T. Ruiz, M. P. Juliarena, R. O. Lezna, E. Wolcan, M. R. Feliz, G. Ferraudi, *Dalton Trans.* **2007**, 2020–2029; d) J. A. Smith, M. W. George, J. M. Kelly, *Coord. Chem. Rev.* **2011**, *255*, 2666–2675; e) A. Saavedra Moncada, E. Gutiérrez-Pineda, I. Maisuls, G. T. Ruiz, A. G. Lappin, G. J. Ferraudi, E. Wolcan, *J. Photochem. Photobiol. A* **2018**, *353*, 86–100.

[3] G. Accorsi, A. Listorti, K. Yoosaf, N. Armaroli, *Chem. Soc. Rev.* **2009**, *38*, 1690–1700.

[4] a) S. Kothavale, N. Sekar, *Dyes Pigments* **2017**, *136*, 31–45; b) Z. Cai, X. Wu, H. Liu, J. Guo, D. Yang, D. Ma, Z. Zhao, B. Z. Tang, *Angew. Chem. Int. Ed.* **2021**, *60*, 23635–23640; c) H.-Y. Yang, H.-Y. Zhang, M. Zhang, H. Zhuo, H. Wang, H. Lin, S.-L. Tao, C.-J. Zheng, X.-H. Zhang, *Chem. Eng. J.* **2023**, *468*, 143721.

[5] a) P. P. Sun, J. P. Duan, J. J. Lih, C. H. Cheng, *Adv. Funct. Mater.* **2003**, *13*, 683–691; b) Q. Sun, P. Yan, W. Niu, W. Chu, X. Yao, G. An, G. Li, *RSC Adv.* **2015**, *5*, 65856–65861; c) I. González, P. Dreyse, D. Cortés-Arriagada, M. Sundararajan, C. Morgado, I. Brito, C. Roldán-Carmona, H. J. Bolink, B. A Loeb, *Dalton Trans.* **2015**, *44*, 14771–14781.

[6] M. Srebro-Hooper, J. Autschbach, *Annu. Rev. Phys. Chem.* **2017**, *68*, 399–420.

[7] Selected references:a) M. Karikomi, C. Kitamura, S. Tanaka, Y. Yamashita, *J. Am. Chem. Soc.* **1995**, *117*, 6791–6792; b) J. Hou, H.-Y. Chen, S. Zhang, G. Li, Y. Yang, *J. Am. Chem. Soc.* **2008**, *130*, 16144–16145; c) H. Zhou, L. Yang, A. C. Stuart, S. C. Price, S. Liu, W. You, *Angew. Chem. Int. Ed.* **2011**, *50*, 2995–2998; d) C. L. Donley, J. Zaumseil, J. W. Andreasen, M. M. Nielsen, H. Sirringhaus, R. H. Friend, J.-S. Kim, *J. Am. Chem. Soc.* **2005**, *127*, 12890–12899; e) Y. Ren, D. Sun, Y. Cao, H. N. Tsao, Y. Yuan, S. M. Zakeeruddin, P. Wang, M. Grätzel, *J. Am. Chem. Soc.* **2018**, *140*, 2405–2408; f) I. Budziak-Wieczorek, L. Ślusarczyk, B. Myśliwa-Kurdziel, M. Kurdziel, M. Srebro-Hooper, I. Korona-Glowniak, M. Gagoś, G. Gładyszewski, A. Stepulak, D. Kluczyk, A. Matwijczuk, *Sci. Rep.* **2022**, *12*, 22140; g) I. Budziak-Wieczorek, D. Kaczmarczyk, K. Rzad, M. Gagoś, A. Stepulak, B. Myśliwa-Kurdziel, D. Karcz, K. Starzak, G. Burdziński, M. Srebro-Hooper, A. Matwijczuk, *Int. J. Mol. Sci.* **2024**, *25*, 3352.

[8] J. Milić, C. Schaack, N. Hellou, F. Isenrich, R. Gershoni-Poranne, S. Egloff, N. Trapp, D. Neshchadin, L. Ruhlmann, C. Boudon, G. Gescheidt, J. Crassous, F. Diederich, *J. Phys. Chem. C* **2018**, *122*, 19100–19109.

[9] T. Biet, K. Martin, J. Hankache, N. Hellou, A. Hauser, T. Bürgi, N. Vanthuyne, T. Aharon, M. Caricato, J. Crassous, N. Avarvari, *Chem. Eur. J.* **2017**, *23*, 437–446.

[10] N. Hellou, M. Srebro-Hooper, L. Favereau, F. Zinna, E. Caytan, L. Toupet, V. Dorcet, M. Jean, N. Vanthuyne, J. A. G. Williams, L. Di Bari, J. Autschbach, J. Crassous, *Angew. Chem. Int. Ed.* **2017**, *56*, 8236–8239.

[11] a) N. Saleh, M. Srebro, T. Reynaldo, N. Vanthuyne, L. Toupet, V. Y. Chang, G. Muller, J. A. G. Williams, C. Roussel, J. Autschbach, J. Crassous, *Chem. Comm.* **2015**, *51*, 3754–3757; b) N. Saleh, D. Kundu, N. Vanthuyne, J. Olesiak-Banska, A. Pniakowska, K. Matczyszyn, V. Y. Chang, G. Muller, J. A. G. Williams, M. Srebro-Hooper, J. Autschbach, J. Crassous, *ChemPlusChem* **2020**, *85*, 2446–2454.

[12] a) E. S. Gauthier, L. Abella, N. Hellou, B. Darquié, E. Caytan, T. Roisnel, N. Vanthuyne, L. Favereau, M. Srebro-Hooper, J. A. G. Williams, J. Autschbach, J. Crassous, *Angew. Chem. Int. Ed.* **2020**, *59*, 8394–8400; b) E. S. Gauthier, L. Abella, E. Caytan, T. Roisnel, N. Vanthuyne, L. Favereau, M. Srebro-Hooper, J. A. G. Williams, J. Autschbach, J. Crassous, *Chem. Eur. J.* **2023**, *29*, e202203477; c) R. Shafei, A. Hamano, C. Gourlaouen, D. Maganas, K. Takano, C. Daniel, F. Neese, *J. Chem. Phys.* **2023**, *159*, 084102; d) see also: V. Giuso, C. Gourlaouen, M. Delporte-Pebay, T. Groizard, N. Vantuyne, J. Crassous, C. Daniel, M. Mauro, *Phys. Chem. Chem. Phys.* **2024**, *26*, 4855–4869.

[13] K. Dhbaibi, L. Favereau, J. Crassous, *Chem. Rev.* **2019**, *119*, 8846–8953.

[14] S. F. Sousa, R. N. Sampaio, N. M. Barbosa Neto, A. E. H. Machado, A. O. T. Patrocinio, *Photochem. Photobiol. Sci.* **2014**, *13*, 1213–1224.

[15] a) M. R. Waterland, K. C. Gordon, J. J. McGarvey, P. M. Jayaweera, *J. Chem. Soc., Dalton Trans.* **1998**, 609–616; b) G. David, P. J. Walsh, K. C. Gordon, *Chem. Phys. Lett.* **2004**, *383*, 292–296.

[16] a) S. O. Obare, C. J. Murphy, *Inorg. Chem.* **2001**, *40*, 6080–6082; b) J. G. Huang, J. Jin, Q. Z. Yuan, X. X. Yang, D. K. Cao, C. Liu, *Inorg. Chem.* **2023**, *62*, 10382–10388; c) W. Guo, B. J. Engelman, T. L. Haywood, N. B. Blok, D. S. Beaudoin, S. O. Obare, *Talanta* **2011**, *87*, 276–283.

[17] N. Saleh, B. Moore II, M. Srebro, N. Vanthuyne, L. Toupet, J. A. G. Williams, C. Roussel, K. K. Deol, G. Muller, J. Autschbach, J. Crassous, *Chem. Eur. J.* **2015**, *21*, 1673–1681.

[18] a) R. López, B. Loeb, D. Striplin, M. Devenney, K. Omberg, T. J. Meyer, *J. Chil. Chem. Soc.* **2004**, *49*, 149–155; b) J. R. Schoonover, W. D. Bates, T. J. Meyer, *Inorg. Chem.* **1995**, *34*, 6421–6422; c) M. K. Kuimova, W. Z. Alsindi, A. J. Blake, E. S. Davies, D. J. Lampus, P. Matousek, J. McMaster, A. W. Parker, M. Towrie, X. Z. Sun, C. Wilson, M. W. George, *Inorg. Chem.* **2008**, *47*, 9857–9869.

[19] A. Chen, S. Meng, J. Zhang, C. Zhang, *Mol. Cryst. Liq. Cryst.* **2014**, *605*, 187–196.

[20] A. Chen, S. Meng, J. Zhang, C. Zhang, *J. Mol. Struct.* **2013**, *1050*, 15–20.

[21] a) H. D. Ludowieg, M. Srebro-Hooper, J. Crassous, J. Autschbach, *Chemistry Open* **2022**, *11*, e202200020; b) T. Mori, P. M. Goumans, E. van Lenthe, F. Wang, *Phys. Chem. Chem. Phys.* **2014**, *16*, 14523–14530; c) E. Yu-Tzu Li, T.-Y. Jiang, Y. Chi, P.-T. Chou, *Phys. Chem. Chem. Phys.* **2014**, *16*, 26184–26192.

[22] a) K. Schmidt, S. Brovelli, V. Coropceanu, D. Beljonne, J. Cornil, C. Bazzini, T. Caronna, R. Tubino, F. Meinardi, Z. Shuai, J.-L. Brédas, *J. Phys. Chem. A* **2007**, *111*, 10490–10499; b) S. Bergwinkl, P. Nuernberger, B. Dick, R. J. Kutta, *ChemPhotoChem* **2024**, *8*, e202300343.

Manuscript received: November 30, 2024
Revised manuscript received: January 19, 2025
Accepted manuscript online: January 21, 2025
Version of record online: February 4, 2025